ACS APPLIED ENERGY MATERIALS

www.acsaem.org
Article

Effects of Metal-Cation Doping on Photocatalytic H_2 Evolution Activity of Layered Perovskite Oxynitride $K_2LaTa_2O_6N$

Hideya Tsuchikado, Shuji Anabuki, Ovidiu Cretu, Yuki Kinoshita, Masashi Hattori, Yuta Shiroma, Dongxiao Fan, Megumi Okazaki, Takuto Soma, Fumitaka Ishiwari, Shunsuke Nozawa, Toshiyuki Yokoi, Michikazu Hara, Koji Kimoto, Akira Yamakata, Akinori Saeki, and Kazuhiko Maeda*

Cite This: ACS Appl. Energy Mater. 2025, 8, 3541−3552

ABSTRACT: Aliovalent cation doping into a heterogeneous photocatalyst affects several of its physicochemical properties, including its morphological characteristics, optical absorption behavior, and charge carrier dynamics, causing a drastic change in its photocatalytic activity. In the present work, we investigated the effects of aliovalent cation doping on the visible-light H_2-evolution photocatalytic activity of the Ruddlesden−Popper layered perovskite oxynitride $K_2LaTa_2O_6N$. The photocatalytic activity toward H_2 evolution from an aqueous NaI solution was found to be enhanced by an increase in the specific surface area of the $K_2LaTa_2O_6N$ photocatalyst, which could be realized upon doping with lower-valence cations (e.g., Mg^{2+}, Al^{3+}, and Ga^{3+}). Among the dopants examined at 1 mol % doping, Ga resulted in the highest activity. The activity of the Ga-doped specimen was further improved with increasing Ga concentration, where the maximal activity was obtained at 10 mol %, corresponding to an apparent quantum yield of 2.7 ± 0.4% at 420 nm from aqueous methanol. This number is the highest reported for a layered oxynitride photocatalyst. In the Ga-doped $K_2LaTa_2O_6N$, a trade-off was observed between the Ga concentration and the photocatalytic activity. Although doping with Ga reduced the particle size of $K_2LaTa_2O_6N$ and suppressed undesirable charge recombination, it led to an enlarged bandgap, unsuitable for visible-light absorption.

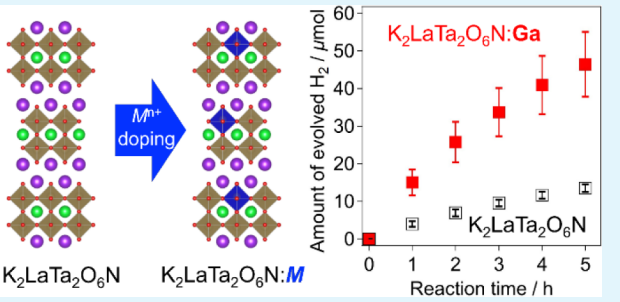

KEYWORDS: *artificial photosynthesis, heterogeneous photocatalysis, mixed-anion compounds, topochemical reaction, visible light*

INTRODUCTION

Solar-driven photocatalytic water splitting is an ideal method for the generation of H_2 as clean chemical energy.[1] Recently, the feasibility of overall water splitting with an external quantum efficiency close to unity was demonstrated using Al-doped $SrTiO_3$ further functionalized with H_2/O_2-evolving cocatalysts.[2] However, its solar-to-hydrogen conversion efficiency remains inevitably low (<0.8%) because of its wide bandgap, although this is high among those reported for photocatalysts that function under simulated sunlight. The large bandgap exceeding 3 eV is an intrinsic issue encountered in most metal oxide photocatalysts that are active toward splitting pure water.[3] The more efficient utilization of solar energy therefore requires the development of a visible-light-responsive photocatalyst.

When nitride anions (N^{3-}) are introduced into a metal oxide, the valence-band edge is shifted negatively because the N 2p orbital has higher energy than the O 2p orbital. This situation results in bandgap narrowing, enabling the absorption of visible light. For example, TaON,[4,5] $SrTaO_2N$,[6] $BaTaO_2N$,[7] $LaTaON_2$,[8] GaN−ZnO solid solution,[9] and $ZnGeN_2$−ZnO solid solution[10] have suitable band edge potentials straddling the water reduction/oxidation potentials.

Here, layered perovskite oxynitrides are promising candidates for visible-light water splitting. Layered metal oxides, especially those with a perovskite structure, are good photocatalysts for UV-driven overall water splitting.[11−15] In general, however, layered perovskite oxynitrides are considered metastable; thus, their synthesis is challenging.[16] Moreover, layered perovskite oxynitrides are sensitive to moisture, which hinders their use in water-splitting systems.[16] For example, although the Ruddlesden−Popper (RP)-phase layered perovskite oxynitride $Li_2LaTa_2O_6N$ combined with a binuclear Ru(II) complex is capable of reducing CO_2 into formate in a nonaqueous environment under visible-light irradiation,[17] $Li_2LaTa_2O_6N$ alone is not stable in aqueous solution. In contrast, $K_2LaTa_2O_6N$, another RP-phase layered perovskite oxynitride, is stable even in aqueous solution and exhibits

Received: December 5, 2024
Revised: February 26, 2025
Accepted: February 28, 2025
Published: March 11, 2025

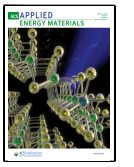

https://doi.org/10.1021/acsaem.4c03131
ACS Appl. Energy Mater. 2025, 8, 3541−3552

visible-light H_2 evolution activity without noticeable degradation.[18] However, its photocatalytic activity (i.e., apparent quantum yield) is unsatisfactory.

The photocatalytic activity of 3D bulk-type perovskite oxynitrides has been reported to be influenced by aliovalent cation dopants.[19−26] Metal-cation doping into an oxynitride also occurs as a result of the formation of a solid solution; for example, compared with pristine $BaTaO_2N$, $BaTaO_2N$−$BaZrO_3$ solid solutions ($0 < Zr/Ta \leq 0.1$ by mole) have been shown to exhibit improved photocatalytic activity toward H_2/O_2 half-cell reactions under visible light.[19] In general, doping with lower-valence cations tends to positively affect the photocatalytic activity of 3D perovskite oxynitrides toward both H_2 and O_2 evolution, as exemplified by $SrNbO_2N$,[20] $SrTaO_2N$,[21,22] $LaTaON_2$,[23] and $BaTaO_2N$;[24,25] however, doping higher-valence tungsten into $BaTaO_2N$ is an exception, resulting in improved O_2 evolution activity.[26] The formation of Ta^{4+} leads to lower photocatalytic activities of Ta-oxynitrides such as Mg-doped $BaTaO_2N$ and Ga-doped $SrTaO_2N$ for O_2 evolution from aqueous $AgNO_3$ with the aid of a CoO_x cocatalyst.[22,24] The ideal oxidation state of Ta in the Ta-oxynitrides is 5+, and reduced Ta^{4+} (and/or Ta^{3+}) was found to be generated during its nitridation from the oxide precursor to the corresponding oxynitride. The thus-produced reduced Ta species act as recombination centers, lowering not only the photocatalytic activity toward O_2 evolution[22] but also that toward H_2 evolution.[27,28] Lower-valence cation doping has also been shown to be effective for improving the activity of the oxysulfide $Y_2Ti_2O_5S_2$ toward H_2 evolution under visible light.[29]

Cation doping to improve photocatalytic activity is much more common in metal oxides than in oxynitrides, and not only electronic effects such as valence/defect control[30,31] but also morphological effects have been reported.[21,32] For example, in $SrTiO_3$, the formation of the reduced Ti species (i.e., Ti^{3+}), which acts as a recombination center, was found to be suppressed by the intentional introduction of oxygen vacancies accompanied by Al^{3+} doping, resulting in an enhancement of the photocatalytic activity.[30] However, the particle size of La-doped $NaTaO_3$ was observably smaller (approximately 0.1−0.7 μm) than that of undoped $NaTaO_3$ (approximately 2−3 μm).[33] In addition, doping of Bi^{3+} into the Ta sites of $NaTaO_3$ has been reported to change the crystal phase and reduce the bandgap, leading to enhanced H_2 evolution activity.[34]

Thus, doping of aliovalent cations into photocatalysts induces several effects, including changing the valence state of the parent cations as well as the morphology and crystal structure of the photocatalyst. However, how the cation doping influences such physicochemical properties and the photocatalytic activity of layered perovskite oxynitrides remains unclear. In the present study, we doped several aliovalent metal cations into $K_2LaTa_2O_6N$ to understand how its photocatalytic activity is influenced by cation doping. The photocatalytic activity of $K_2LaTa_2O_6N$ toward H_2 evolution has been reported to be improved by temperature control during the synthesis of the precursor oxide[28] as well as by interlayer modification of organic molecules.[35]

Here, we demonstrate that doping of metal cations into $K_2LaTa_2O_6N$ is not only another effective strategy for improving its photocatalytic activity but also imparts the doped $K_2LaTa_2O_6N$ with physicochemical properties that differ from those of doped bulk-type oxynitrides. A unique relationship between the physicochemical properties of the doped $K_2LaTa_2O_6N$ and their photocatalytic activities, which is distinct from those already reported in 3D-bulk perovskite oxynitride photocatalysts, is reported.

EXPERIMENTAL SECTION

Materials. Cs_2CO_3 (≥99.5%; Kanto Chemical), $La(NO_3)_3 \cdot 6H_2O$ (≥99.0%; Kanto Chemical), Ta_2O_5 (≥99.9%; Wako Pure Chemicals), MgO (>98.0%; Wako Pure Chemicals), Al_2O_3 (>99.0%; Soekawa Rikagaku), Ga_2O_3 (>99.99%; Kojundo Chemical Lab.), ZrO_2 (>99.0%; Kanto Chemical), MoO_3 (>99.5%; Kanto Chemical), WO_3 (>99.99%; Kojundo Chemical Lab.), methanol (>99.8%; Kanto Chemical), KNO_3 (≥99.0%; Wako Pure Chemicals), K_2CO_3 (≥99.5%; Kanto Chemical), NaI (≥99.5%; Kanto Chemical), H_2SO_4 (≥96.0%; Kanto Chemical), and $[Pt(NH_3)_4]Cl_2 \cdot H_2O$ (99% (99.95% Pt); Wako Pure Chemicals) were used as received.

Synthesis of Cation-Doped $K_2LaTa_2O_6N$. $CsLaTa_2O_7$ was synthesized by a flux method. Cs_2CO_3, $La(NO_3)_3 \cdot 6H_2O$, and Ta_2O_5 were mixed in a Cs/La/Ta molar ratio of 10/1/2 in an agate mortar using a small amount of methanol. The 10-fold excess amount of Cs was used as a flux and to compensate for losses of Cs due to volatilization. For $CsLaTa_2O_7$ doped with the aliovalent metal cations (M), the corresponding metal oxides were added to the mixture such that the Cs/La/Ta/M molar ratio was $10/1/2-0.02x/0.02x$ (x = 1, 5, 10, 20). The precursor mixture containing Cs, La, Ta, and M was transferred to an alumina crucible and then heated at 973 K for 24 h (ramp: 2 K min^{-1}) under air in a furnace. The resultant solid was washed thoroughly with water to remove residues and then dried at 343 K in an oven. The obtained powder samples are abbreviated as $CsLaTa_2O_7$:M, where the x value (i.e., the dopant concentration parameter) is 1 unless otherwise stated.

$KLaTa_2O_7$:M was prepared from $CsLaTa_2O_7$:M in molten KNO_3 via a K^+/Cs^+ ion-exchange reaction. The obtained $CsLaTa_2O_7$:M (4.3 mmol) was mixed with KNO_3 (43 mmol), and the resultant mixture was heated at 673 K for 48 h in air. The obtained powder was washed with water repeatedly to remove remaining KNO_3, then dried at 343 K in an oven.

Finally, the $KLaTa_2O_7$:M samples were nitridated to $K_2LaTa_2O_6N$:M. Each of the resultant $KLaTa_2O_7$:M (1.5 mmol) samples was mixed with K_2CO_3 (1.1 mmol), and the mixtures were heated at 1173 K for 3 h under a 50 mL min^{-1} NH_3 gas flow (≥99.9995%; Sumitomo Seika Chemicals). The overall synthesis route is depicted in Scheme 1.

Scheme 1. Synthesis of $CsLaTa_2O_7$:M, $KLaTa_2O_7$:M, and $K_2LaTa_2O_6N$:M

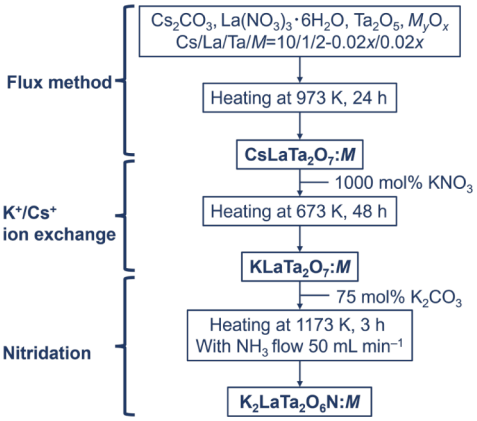

https://doi.org/10.1021/acsaem.4c03131
ACS Appl. Energy Mater. 2025, 8, 3541−3552

Loading Pt Cocatalyst. Pt was loaded as a water-reduction cocatalyst onto the $K_2LaTa_2O_6N$:*M* via an impregnation−H_2 reduction method. The nominal amount of Pt was fixed to be 1 wt % to exclude any factor other than Pt loading amount. $K_2LaTa_2O_6N$:*M* was dispersed in an aqueous solution containing the required amount of $[Pt(NH_3)_4]Cl_2$ to obtain 1 wt % of Pt on $K_2LaTa_2O_6N$:*M*. The solution was evaporated to dryness in air, and the resultant solid mixture was heated at 473 K for 1 h under 20 mL min^{-1} H_2 gas flow.

General Characterization. X-ray diffraction (XRD) patterns were acquired using a powder X-ray diffractometer (Rigaku MiniFlex600) equipped with a Cu Kα radiation source operating at 40 kV and 15 mA. In this work, the position of the XRD peak may vary by ∼0.2° due to an experimental error, even for the same sample. The surface morphology of the samples was observed by field-emission scanning electron microscopy (FE-SEM; Hitachi S-5500). The chemical composition of the $K_2LaTa_2O_6N$:*M* samples were analyzed by X-ray fluorescence (XRF) spectroscopy and scanning electron microscopy (SEM; JEOL JSMIT100LA) in conjunction with energy-dispersive X-ray spectroscopy (EDS). UV−visible diffuse-reflectance spectra of the $K_2LaTa_2O_6N$:*M* samples were acquired using a spectrophotometer (JASCO V-770) equipped with an integrating sphere; $BaSO_4$ was used as a reference. The Brunauer−Emmett−Teller (BET) surface area was estimated using a BELSORP max II (MicrotracBEL) at liquid-N_2 temperature (77 K). X-ray absorption spectroscopy measurements were conducted at the BL-9C beamline of the Photon Factory (Proposal No. 2022G676),[28] where the Ta L_3-edge and Ga K-edge absorption of $K_2LaTa_2O_6N$:*M* specimens and reference samples were recorded at room temperature. The analysis of the obtained X-ray absorption fine structure (XAFS) was conducted using the Athena software package.[36] X-ray photoelectron spectroscopy (XPS) was performed using ESCA-3400 and ESCA-3200 X-ray photoelectron spectrometers (Shimadzu). The obtained binding-energy values were calibrated for each sample by the C 1s peak (285.0 eV) as a reference. Scanning transmission electron microscopy (STEM) observations were conducted in a manner similar to those in previous works with almost identical conditions using a Themis Z transmission electron microscope (Thermo Fisher Scientific).[35]

Time-Resolved Microwave Conductivity (TRMC) Measurements. TRMC measurements of the prepared samples were performed at room temperature in air according to the method described previously.[37] The powdered $K_2LaTa_2O_6N$:*M* samples were fixed onto quartz substrates by transparent adhesive tape, which does not interfere with any TRMC signals. The microwave power and frequency were ∼3 mW and ∼9 GHz, respectively. The light source for the excitation was the third harmonic generation (355 nm) of a Nd:YAG laser (Continuum Surelite II, 5−8 ns pulse duration, 10 Hz). The photoconductivity $\Delta\sigma$ was calculated using

$$\Delta\sigma = A^{-1}\Delta P_r P_r^{-1} \quad (1)$$

where A, ΔP_r, and P_r are the sensitivity factor, the transient power change of the reflected microwaves, and the power of the reflected microwaves, respectively. The obtained $\Delta\sigma$ was converted into the product of the quantum yield (φ) and the sum of the charge carrier mobilities $\Sigma\mu$ ($= \mu_+ + \mu_-$) using

$$\varphi\Sigma\mu = \Delta\sigma(eI_0F_{light})^{-1} \quad (2)$$

where e, I_0, and F_{light} are the elementary charge (1.6×10^{-19} C), incident photon density, and filling factor, respectively. Here, I_0 was 9.1×10^{15} photons cm^{-2} $pulse^{-1}$.

Transient Absorption Spectroscopy. Transient absorption was observed using a custom-made spectrometer described in a previous report.[38] The details of the procedure are given elsewhere.[39] $K_2LaTa_2O_6N$ samples (1.5 mg cm^{-2}) were loaded onto a CaF_2 plate that transmits. The samples were photoexcited using 355 nm pulses from a Nd:YAG laser (Continuum Surelite; duration, 6 ns; power, 0.5 mJ; repetition rate, 5 Hz) The observations were conducted in a 20 Torr N_2 atmosphere.

Photocatalytic Reactions. The photocatalytic activity of Pt/$K_2LaTa_2O_6N$:*M* was evaluated at room temperature using a conventional closed circulation gas system, where 50 mg of the obtained Pt/$K_2LaTa_2O_6N$:*M* was suspended in a 5 mM NaI aqueous solution (140 mL, pH 2.5). After the gas in the reaction cell was withdrawn, a small amount (∼3 kPa) of Ar was introduced. The suspension was exposed to the radiation of a 300 W xenon lamp equipped with both a mirror (CM-1) and a cutoff filter (L42). The evolved gases were quantitated by gas chromatography (Shimadzu GC-8A equipped with a TCD detector and an MS-5A column).

The apparent quantum yield (AQY) for H_2 evolution was measured in an aqueous methanol solution (10 vol%) or NaI solution (5 mM) using a previously reported method[35] to minimize any adverse effect of backward reactions involving oxidized donor species; the AQY was calculated using the equation:

$$\mathrm{AQY}(\%) = (2 \times R/I) \times 100 \quad (3)$$

where R and I represent the rate of H_2 evolution and the rate of incident photons, respectively. Here, the light source was a 300 W xenon lamp with monochromatic visible light (λ = 420 nm) whose total intensity ranged from 22 to 25 mW.

RESULTS AND DISCUSSION

Structural Characterization of $K_2LaTa_2O_6N$:*M*. The synthesized $K_2LaTa_2O_6N$:*M* samples with 1 mol % dopant were investigated by XRD measurements. Figure 1 shows XRD

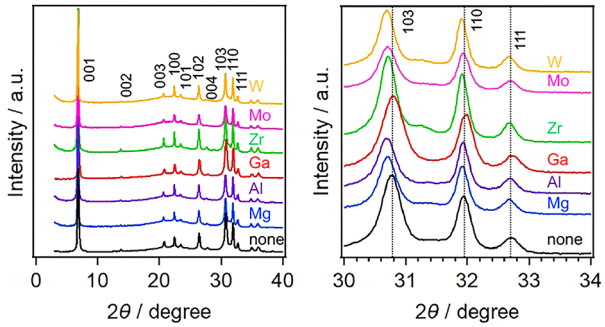

Figure 1. XRD patterns for $K_2LaTa_2O_6N$ and $K_2LaTa_2O_6N$:*M*(1 mol %). The right panel is a magnified image of the 2θ region from 30° to 34°.

patterns for $K_2LaTa_2O_6N$ and $K_2LaTa_2O_6N$:*M*. The reflections from the undoped $K_2LaTa_2O_6N$ were assigned using the crystallographic data reported elsewhere.[17] The XRD patterns for all of the $K_2LaTa_2O_6N$:*M* samples match that for $K_2LaTa_2O_6N$, indicating that doping with metal cations at 1 mol % did not affect the crystal structure of the resultant

https://doi.org/10.1021/acsaem.4c03131
ACS Appl. Energy Mater. 2025, 8, 3541−3552

Table 1. Bulk and Surface Atomic Compositions in $K_2LaTa_2O_6N$:*M*(1 mol %)

	Bulk[a]		Surface[b]			
Dopant in $K_2LaTa_2O_6N$	K/La	Ta/La	K/La	Ta/La	N/La	Ta^{4+}/Ta^{5+}
Nominal	2	2	2	2	1	0
Nominal (doped)	2	1.98	2	1.98	-	0
None	1.67 ± 0.1	1.94 ± 0.07	5.4	2.3	1.7	2.0
Mg	1.11 ± 0.06	1.98 ± 0.08	15.6	2.0	1.3	3.4
Al	1.48 ± 0.1	1.75 ± 0.09	4.3	2.3	1.3	0.5
Ga	1.63 ± 0.01	1.93 ± 0.03	6.0	2.2	1.2	1.7
Zr	1.50 ± 0.1	1.76 ± 0.07	15.2	2.3	1.5	0.9
Mo	1.55 ± 0.08	1.80 ± 0.07	5.0	1.7	1.4	3.0
W	1.58 ± 0.07	1.91 ± 0.04	5.7	1.8	1.5	1.9

[a]Determined by SEM-EDS. The atomic ratios were calculated from the average values for each sample by measuring at least six different points. [b]Determined by XPS.

oxynitride. Upon metal-cation doping, a somewhat complicated peak shift was observed. Although the 111 reflections for the various $K_2LaTa_2O_6N$:*M* (*M* = Mg, Al, Ga, Zr, Mo, W) samples are located at approximately the same position (2θ = 32.7°), the 103 reflections (except that for $K_2LaTa_2O_6N$:Ga) are shifted toward lower 2θ angles compared with those for the undoped $K_2LaTa_2O_6N$, indicating an expansion of the crystal lattice according to Bragg's law ($2d\sin\theta = n\lambda$). A lower-angle shift similar to that observed for the 103 reflections was also observed for the 110 reflections, although the magnitude of the shift was not as pronounced as that for the 103 reflections. Given the ionic radii of the doped cations (Table S1), shifts to lower angles are expected in the patterns for $K_2LaTa_2O_6N$:Mg and $K_2LaTa_2O_6N$:Zr, whereas shifts to higher angles are expected in the patterns for the other samples. One possible explanation for the observed peak shifts showing peculiar behavior for each crystal face is that the doped cation species in the $K_2LaTa_2O_6N$ host are somewhat unevenly distributed in the crystal for each cation species; of course, the experimental error as mentioned in the experimental section should be taken into account. In addition, if the size of the cation species substituted as a result of doping is similar to that of the dopant and/or if the doping concentration is low, the diffraction peak shift may not be observable.[29]

The atomic concentrations of K, La, and Ta in the $K_2LaTa_2O_6N$:*M* samples were determined by EDS analysis. As listed in Table 1, the Ta/La atomic ratios were close to the ideal value; however, the K/La ratios were obviously smaller than expected, indicating that interlayer protonation may have occurred for charge compensation.[18] The Ta/La and K/La ratios obtained from XRF measurement were close to those measured by EDS analysis (Table S2).

The morphology of $K_2LaTa_2O_6N$:*M* was observed by SEM. As shown in Figure 2, all the samples are composed of well-crystallized lamellar particles, reflecting their layered structure. The lateral sizes of the Mg- and Ga-doped specimens were obviously smaller than those of the other specimens; this observation is further supported by the results of specific surface area measurements. The specific surface areas of the Mg- and Ga-doped specimens were 4.1 and 5.4 $m^2\ g^{-1}$, which are larger than those of the other specimens. The Al-doped specimen also exhibited a larger specific surface area (3.5 $m^2\ g^{-1}$) compared with that of the undoped material (2.4 $m^2\ g^{-1}$). By contrast, doping with Zr, Mo, or W did not result in an increase of the specific surface area.

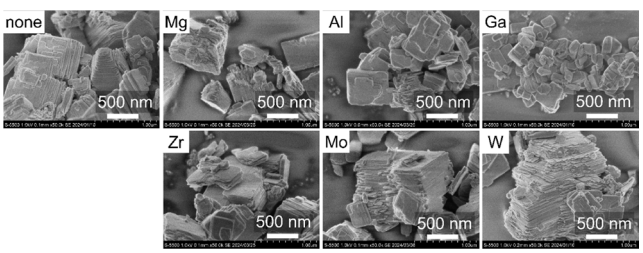

Figure 2. SEM images of $K_2LaTa_2O_6N$ and $K_2LaTa_2O_6N$:*M* (1 mol %).

Thus, metal-cation doping into $K_2LaTa_2O_6N$ caused a morphological change despite the low nominal dopant concentration (1 mol %); in particular, doping with lower-valence cations was found to reduce the particle size of $K_2LaTa_2O_6N$. It is empirically known that doping of lower valence cations leads to particle size reduction of the host material, as exemplified by Zr-doped Ta_2O_5,[40] Zr-doped $BaTaO_2N$[41] and Mg-doped $BaTaO_2N$.[24] It has been also pointed out that cation doping does not always result in the particle size reduction, especially when higher valence cations are doped. For example, the average particle size of $CaTiO_3$:La synthesized by a flux method depended on the concentration of the La dopant; the La concentration smaller than 1 mol % contributed to an increase in the average particle size.[42] The characteristic crystal growth depending on the dopant concentration has been reported for $SrTiO_3$:*M* (*M* = Y, La, Nd, Ho, Nb and Sb),[43,44] and is known as an anomaly of grain growth of donor-doped perovskite materials, so-called "donor anomaly".[45]

Based on these previous results, the fact that the particle size of $K_2LaTa_2O_6N$ was reduced upon lower valence cations could be explained by the crystal growth suppression effect by the dopant. On the other hand, the particle growth observed in the Mo- and W-doped $K_2LaTa_2O_6N$ may be related to the donor anomaly effect.

Valence State and Optical Properties of $K_2LaTa_2O_6N$:*M*. We acquired X-ray absorption near edge structure (XANES) spectra to investigate the local structure and bulk valence of Ta in the $K_2LaTa_2O_6N$:*M* samples. Figure S1 shows Ta L_3-edge XANES spectra of $K_2LaTa_2O_6N$:*M*. All of the $K_2LaTa_2O_6N$:*M* spectra well match that of $K_2LaTa_2O_6N$. This result demonstrates that the local structures around Ta atoms in these samples are identical to each other even after doping, consistent with the XRD analysis results (Figure 1).

We acquired K 2p, La 3d, Ta 4f, and N 1s XPS spectra of the $K_2LaTa_2O_6N$:*M* samples (Figure 3) to investigate the surface

https://doi.org/10.1021/acsaem.4c03131
ACS Appl. Energy Mater. 2025, 8, 3541−3552

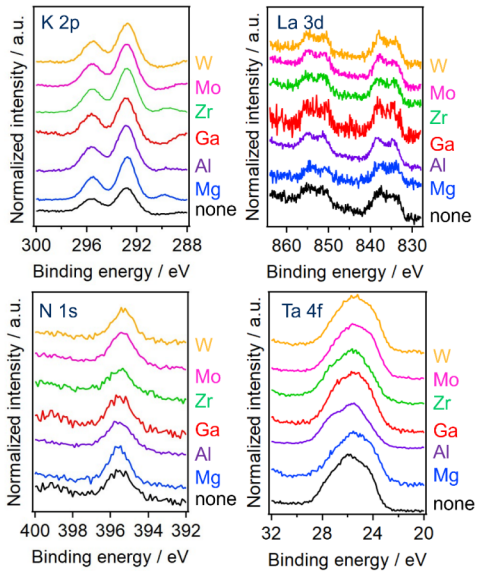

Figure 3. K 2p, La 3d, N 1s, and Ta 4f XPS spectra of $K_2LaTa_2O_6N$ and $K_2LaTa_2O_6N$:*M*(1 mol %).

valence states of consistent elements. All of the spectra were calibrated on the basis of the C 1s peak at 285.0 eV. The peak positions of K 2p, La 3d, and N 1s are approximately the same irrespective of the doped cations. By contrast, the Ta 4f peak positions clearly change depending on the dopant. The Ta 4f XPS spectrum essentially gives two distinct peaks due to $4f_{5/2}$ and $4f_{7/2}$ photoelectrons.[46] However, the presence of reduced Ta species such as Ta^{4+} or Ta^{3+} obscures the two peaks.[28] Curve-fitting analysis of the Ta 4f XPS spectra reveals that the surface Ta^{4+}/Ta^{5+} atomic ratio was relatively small in the Al and Zr samples (Figure S2 and Table 1). By contrast, the surface Ta^{4+}/Ta^{5+} ratios for the Mg and Mo analogues were larger than that for the undoped sample. Thus, the metal-cation doping affected the surface atomic Ta^{4+}/Ta^{5+} ratio, which is associated with the photocatalytic activity of undoped $K_2LaTa_2O_6N$ toward H_2 evolution.[28]

The surface atomic compositions of the $K_2LaTa_2O_6N$:*M* particles were calculated on the basis of the corresponding XPS peak areas (Table 1). Although the bulk K concentration was lower than the ideal value, the surface K concentration was much larger. The surface N/La atomic ratio was also estimated from the corresponding XPS peak areas, which showed that the surface N/La values were larger than the ideal value in all cases. These results suggest that K and N species are segregated near the surface of $K_2LaTa_2O_6N$:*M*. We also observed that, among the doped samples, the N/La atomic ratios in the $K_2LaTa_2O_6N$:*M* samples were low when lower-valence cations (e.g., Mg, Al, and Ga) were used but were large (e.g., Zr, Mo, and W) for higher-valence cations.

The optical properties of the $K_2LaTa_2O_6N$:*M* samples were evaluated by UV−visible DRS (Figure 4). All of the prepared samples except for $K_2LaTa_2O_6N$:Ga absorb visible light at wavelengths as long as ∼600 nm. However, the absorption edge of $K_2LaTa_2O_6N$:Ga was blue-shifted by ∼50 nm compared with the absorption edges of the other samples. This shift is likely attributable to $K_2LaTa_2O_6N$:Ga having the lowest N content among the investigated samples (Table 1) because the valence-band maximum for the $K_2LaTa_2O_6N$ host is formed by N 2p orbitals.

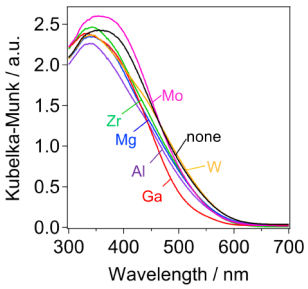

Figure 4. UV−visible DRS spectra of $K_2LaTa_2O_6N$ and $K_2LaTa_2O_6N$:*M*(1 mol %).

Photocatalytic Activity of $K_2LaTa_2O_6N$:*M*. The H_2-evolution activity of $K_2LaTa_2O_6N$:*M* with a Pt cocatalyst was evaluated in an aqueous solution containing NaI. The time courses of H_2 evolution are shown in Figure 5. All of the

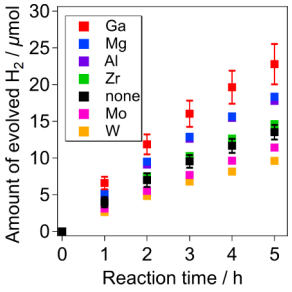

Figure 5. Time courses of H_2 evolution over Pt/$K_2LaTa_2O_6N$:*M*(1 mol %) under visible light (λ > 400 nm). Reaction conditions: catalyst, 50 mg; reactant solution, 5 mM aqueous NaI solution (pH 2.5, 140 mL); light source, 300 W xenon lamp with a cutoff filter (L42).

$K_2LaTa_2O_6N$:*M* samples exhibited activity under visible-light irradiation; however, the trend varied depending on the dopant. Doping with lower-valence cations (i.e., Mg, Al, and Ga) resulted in enhanced activity relative to that of the undoped analogue, whereas doping with Zr did not affect the activity. Among the investigated dopants, Ga was found to result in the photocatalyst with the highest activity. By contrast, doping with higher-valence cations (i.e., Mo and W) resulted in lower activity.

Effects of Ga Doping Concentration. Given the enhanced activity of $K_2LaTa_2O_6N$:Ga (1 mol %), we further investigated the effect of Ga doping by varying the nominal Ga concentration. XRD patterns for $K_2LaTa_2O_6N$:Ga with different Ga concentrations are presented in Figure 6a. The reflections for the $K_2LaTa_2O_6N$:Ga samples were assigned to single-phase $K_2LaTa_2O_6N$, indicating that the crystal structure of the products remained unchanged upon doping with Ga at nominal concentrations as high as 20 mol %. Similar to the XRD data for $K_2LaTa_2O_6N$:*M* (1 mol %) samples (Figure 1), peculiar peak shifts for each crystal face were seen (the right panel of Figure 6a). It should be noted that the ionic radius of Ga^{3+} (0.62 A) is very similar to that of Ta^{5+} (0.64 A). As will be discussed later, the actual concentration of doped Ga^{3+} was less than the nominal value. Thus, it was difficult to discuss the XRD peak position of $K_2LaTa_2O_6N$:Ga with different Ga concentrations. The phenomenon of no XRD peak shift despite aliovalent cation doping has also been reported in Mg-doped $BaTaO_2N$.[47]

https://doi.org/10.1021/acsaem.4c03131
ACS Appl. Energy Mater. 2025, 8, 3541−3552

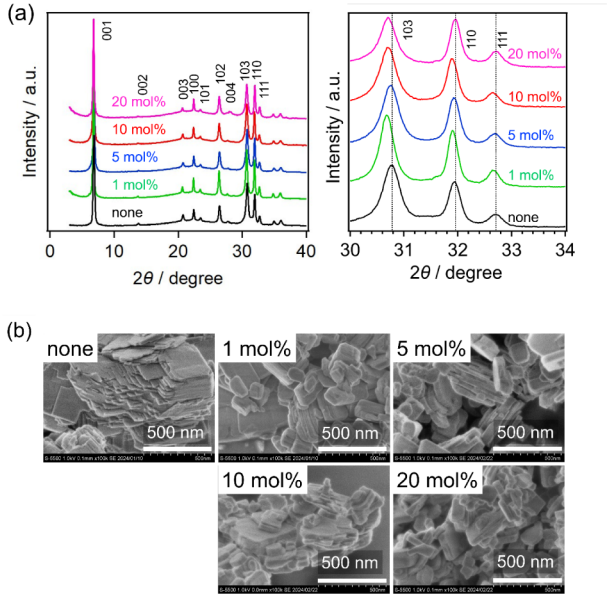

Figure 6. (a) XRD patterns for $K_2LaTa_2O_6N$:Ga (0, 1, 5, 10, 20 mol %). The right panel shows a magnified image of the 2θ range from 30° to 34°. (b) SEM images of the same samples.

SEM images of the same samples are shown in Figure 6b. The $K_2LaTa_2O_6N$:Ga samples exhibit a smaller particle size than the undoped specimen; however, little difference is observed among the different Ga-doped specimens. Nevertheless, the specific surface areas tended to increase with increasing Ga concentration: from 5.4 $m^2\ g^{-1}$ for the 1 mol % sample to 6–7 $m^2\ g^{-1}$ for the ≥5 mol % samples.

High-angle annular dark-field (HAADF) STEM images taken along the [100] and [001] directions of $K_2LaTa_2O_6N$:Ga (10 mol %) are shown in Figure 7a. Here, the signal intensity in a HAADF-STEM image is approximately proportional to Z^2, where Z represents the atomic number of the elements.[48] Thus, heavier atoms such as ^{57}La and ^{73}Ta in the HAADF images are observed as brighter dots. The arrangement of these brighter dots in the HAADF images is consistent with that expected from the crystal structure of $K_2LaTa_2O_6N$. To investigate the location of the Ga dopant atoms, we conducted a STEM-EDS mapping analysis (Figure 7b,c). The results revealed that the location of Ga was overlapped with that of Ta, strongly suggesting the successful substitution of Ga for Ta in the perovskite block.

The atomic compositions of the $K_2LaTa_2O_6N$:Ga samples are listed in Table 2. EDS measurements revealed that the K concentration was lower than that expected from the stoichiometry, irrespective of the level of Ga doping, and tended to decrease with increasing doping level. By contrast, the Ta concentration was close to the ideal value. We determined the actual Ga concentration by conducting XRF measurements (Figure S3). The concentration of Ga dopant in $K_2LaTa_2O_6N$:Ga was 20–40% of the nominal concentration, although it increased with increasing nominal concentration. XRF measurements also revealed that the Ga concentration was already lower in the oxide precursor of $CsLaTa_2O_7$:Ga and remained unchanged upon K^+/Cs^+ exchange and subsequent topochemical nitridation (Figure S4).

The substitution of Ga atoms at the six-coordinated Ta site in the perovskite block was supported by XANES measurements. Figure S5 shows Ga K-edge XANES spectra of $K_2LaTa_2O_6N$:Ga (10 mol %) and $KLaTa_2O_7$:Ga (10 mol %). The XANES spectrum of β-Ga_2O_3 is also shown for reference. In the XANES spectrum of β-Ga_2O_3, two peaks attributed to tetrahedrally and octahedrally coordinated Ga sites[49] appear at ~10375 and ~10379 eV, respectively. However, the XANES spectra of both $K_2LaTa_2O_6N$:Ga (10 mol %) and $KLaTa_2O_7$:Ga (10 mol %) show only a single

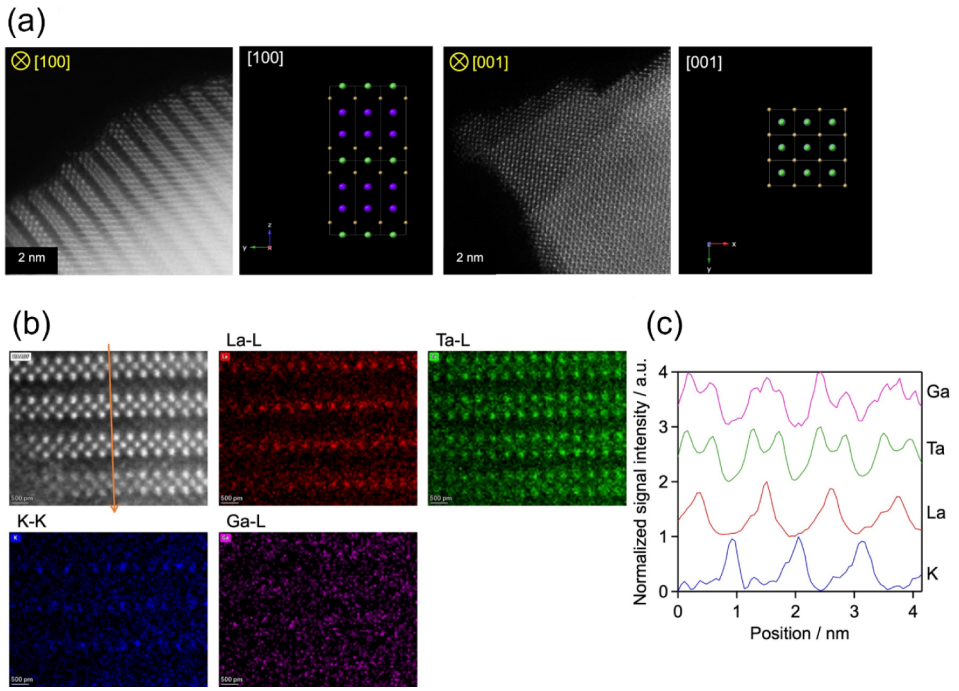

Figure 7. (a) HAADF-STEM images of $K_2LaTa_2O_6N$:Ga (10 mol %). Color code: K^+, purple; La^{3+}, green; Ta^{5+}, yellow. (b) Magnified HAADF-STEM image and EDS mapping images. (c) Line mapping along the direction indicated by the orange arrow in panel b.

https://doi.org/10.1021/acsaem.4c03131
ACS Appl. Energy Mater. 2025, 8, 3541–3552

Table 2. Bulk and Surface Atomic Compositions in $K_2LaTa_2O_6N$:Ga (0, 1, 5, 10, 20 mol %)

	Bulk			Surface[a]				
Ga/mol %	K/La[b]	Ta/La[b]	Ga/La[c]	K/La	Ta/La	Ga/La	N/La	Ta^{4+}/Ta^{5+}
x	2	2−0.02x	0.02x	2	2−0.02x	0.02x	-	-
0	1.67 ± 0.1	1.94 ± 0.07	0	5.4	2.3	0	1.7	2.0
1	1.32 ± 0.07	1.87 ± 0.1	0.0078	6.0	2.2	<0.01	1.2	1.7
5	1.13 ± 0.05	2.01 ± 0.06	0.026	3.3	2.1	0.01	1.0	0.6
10	1.05 ± 0.05	1.88 ± 0.06	0.043	5.1	2.0	0.01	1.1	0.8
20	0.80 ± 0.05	1.56 ± 0.08	0.16	2.7	1.3	0.37	0.5	0.4

[a]Determined by XPS. [b]Determined by SEM-EDS. The atomic ratios were calculated from the average values for each sample by measuring at least six different points. [c]Determined by XRF.

component, indicating that the Ga atoms have octahedral coordination. The results therefore suggest that Ga was successfully substituted at Ta sites in both the oxynitride and the oxide precursor, consistent with the HAADF/STEM observations (Figure 7).

The surface atomic compositions of the $K_2LaTa_2O_6N$:M particles determined by XPS analysis are listed in Table 2. The surface K concentration was larger, similar to the $K_2LaTa_2O_6N$:*M*(1 mol %) series. The surface Ta/La atomic ratio for $K_2LaTa_2O_6N$:Ga was slightly higher than expected from the stoichiometry, indicating a Ta-rich environment at the material surface. However, $K_2LaTa_2O_6N$:Ga(20 mol %) gave a Ta/La ratio of 1.3, which is lower than the expected value. $K_2LaTa_2O_6N$:Ga(20 mol %) exhibited the highest Ga/La surface concentration (0.37) among the investigated samples, which was much higher than the expected value, indicative of the segregation of Ga species in the surface region. This is also clear from the fact that the surface Ga/La ratio was much higher than the bulk Ga/La ratio. The trend of the surface N/La atomic ratio was similar to that of the surface Ta/La ratio.

Ga doping into $K_2LaTa_2O_6N$ altered the valence state of surface Ta species, although no significant change was observed for the XPS peak positions in the K 2p, La 3d, and N 1s spectra (Figures 8, S6 and S7). The Ta $4f_{5/2}$ and $4f_{7/2}$

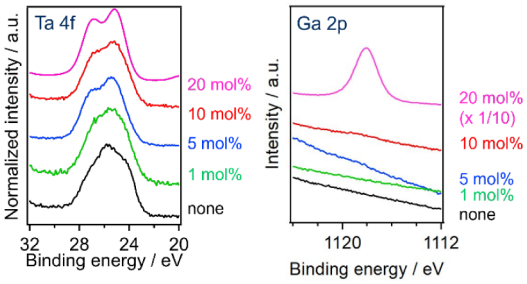

Figure 8. Ta 4f and Ga 2p XPS spectra of $K_2LaTa_2O_6N$:Ga (0, 1, 5, 10, 20 mol %).

peaks tended to become sharper with increasing Ga concentration, accompanied by a decrease in the Ta^{4+}/Ta^{5+} surface atomic ratio (Figure S8). Although no photoelectron signal from Ga could be detected for the 1 mol % doped sample, a clear Ga signal was observed in the spectra of samples with higher Ga concentrations. The binding energy for the Ga $2p_{3/2}$ peak for $K_2LaTa_2O_6N$:Ga with higher Ga concentrations was 1118.0−1118.2 eV, which is lower than that for Ga_2O_3 (1118.9 eV)[50,51] but higher than that for GaN (1117.1 eV[52] and 1117.6 eV[53]). These results indicate that the Ga dopant was coordinated by both O^{2-} and N^{3-} ions.

UV−visible DRS spectra of $K_2LaTa_2O_6N$:Ga with different Ga concentrations are shown in Figure 9. As already

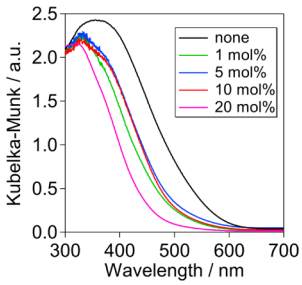

Figure 9. UV−visible DRS spectra of $K_2LaTa_2O_6N$:Ga (0, 1, 5, 10, 20 mol %).

mentioned for the spectra of the 1 mol % sample, the spectra of the samples with ≥5 mol % doping showed a clear blueshift of the absorption edge. The absorption edges for the samples with 1, 5, and 10 mol % were almost the same (i.e., 500 nm). However, $K_2LaTa_2O_6N$:Ga (20 mol %) showed a more pronounced blueshift of the absorption edge. These results indicate that the bandgap of $K_2LaTa_2O_6N$ was enlarged by heavy doping with Ga.

The enlarged bandgap of $K_2LaTa_2O_6N$ as a result of Ga doping is attributed to the reduced concentration of N (Table 2), which weakens the contribution to the formation of the upper part of the valence band. Another possible explanation for the enlarged bandgap is a size effect. The results of our previous study suggested that $K_2LaTa_2O_6N$ exhibits a bandgap reduction with increasing particle size even though the N concentration decreases.[28] This can be explained by orbital−orbital overlap within large 2D polyanion $LaTa_2O_6N^{2-}$ sheets, which increases the bandwidth, thereby leading to a smaller bandgap. As displayed in Figure 6b, doping $K_2LaTa_2O_6N$ with Ga caused a reduction of the particle size. Therefore, the substantial blueshift of the absorption edge for $K_2LaTa_2O_6N$ upon Ga doping may be associated with the reduced particle size to a certain extent.

We next evaluated the H_2 evolution activity of $K_2LaTa_2O_6N$:Ga. As shown in Figure 10, all of the $K_2LaTa_2O_6N$:Ga samples exhibited higher H_2 evolution activity than undoped $K_2LaTa_2O_6N$; however, the activity varied with the Ga concentration. The photocatalytic activity was enhanced as the Ga concentration was increased to 10 mol %. However, the activity decreased for Ga doping at 20 mol %. The AQY for the optimized $K_2LaTa_2O_6N$:Ga (10 mol %) sample was 2.7 ± 0.4% at 420 nm (Figure S9). We previously reported that the photocatalytic activity of $K_2LaTa_2O_6N$ for visible-light H_2 evolution could be improved via an appropriate

https://doi.org/10.1021/acsaem.4c03131
ACS Appl. Energy Mater. 2025, 8, 3541−3552

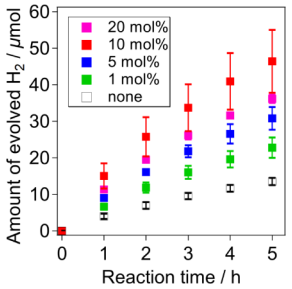

Figure 10. Time courses of H_2 evolution over Pt/$K_2LaTa_2O_6N$:Ga under visible light (λ > 400 nm). Reaction conditions: catalyst, 50 mg; reactant solution, 5 mM aqueous NaI solution (pH 2.5, 140 mL); light source, 300 W xenon lamp with cutoff filter (L42).

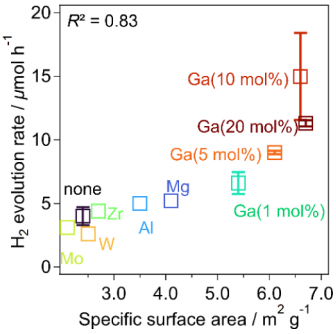

Figure 11. Relationship between specific surface area and H_2 evolution rate for $K_2LaTa_2O_6N$:*M*.

interlayer modification, giving an AQY of 2.0% at 420 nm with aqueous methanol.[35] We also emphasize that most of the visible-light-responsive semiconductors, which include Rh-doped $SrTiO_3$,[54] ZrO_2-modified TaON,[55] $ATaO_2N$ (*A* = Ca, Sr, Ba)[56] and polymeric carbon nitride,[57] themselves have not given a measurable AQY for H_2 evolution in aqueous NaI, due primarily to the undesirable backward reactions involving oxidized I^- species (e.g., IO_3^- and I_3^-). By contrast, the $K_2LaTa_2O_6N$:Ga (10 mol %) exhibited a maximum AQY of 1.3% at 420 nm from an aqueous NaI solution. Thus, the present metal-cation doping approach is an effective strategy for improving the visible-light H_2 evolution activity of $K_2LaTa_2O_6N$.

In heterogeneous (photo)catalysis, turnover number (i.e., the number of product molecules divided by that of catalytic sites) should be used as an indicator of stability.[1] As $K_2LaTa_2O_6N$:*M* alone did not produce H_2, the active site for H_2 evolution was Pt. Therefore, the turnover number can be calculated based on Pt. Because the amount of Pt loaded in the 1 wt % Pt/$K_2LaTa_2O_6N$:Ga (10 mol %) was approximately 2.6 μmol, the turnover number for H_2 evolution was calculated to be 18.

Factors Affecting Photocatalytic Activity of Metal-Cation-Doped $K_2LaTa_2O_6N$. The photocatalytic activity of the $K_2LaTa_2O_6N$:*M* depended not only on the dopant element but also on the concentration of the dopant. From the results of specific surface area measurements, we found a good correlation between the specific surface area and the H_2 evolution rate for $K_2LaTa_2O_6N$:*M* samples (Table 3 and Figure 11); that is, increasing the specific surface area leads to a higher H_2 evolution rate.

The presence of reduced Ta species such as Ta^{4+} and Ta^{3+} is known to adversely affect the photocatalytic activity of Ta-based oxynitrides for H_2 evolution.[4,22,27,55,58] A similar situation is observed for undoped $K_2LaTa_2O_6N$.[28] In the present work, the Ta^{4+}/Ta^{5+} ratios for $K_2LaTa_2O_6N$:*M* calculated by XPS analysis are listed in Table 3. As shown in Figure S10a, no strong relation was found between the Ta^{4+}/Ta^{5+} ratio (more specifically, its inverse value) and the H_2 evolution activity (R^2 = 0.27). However, the product of the inverse of the Ta^{4+}/Ta^{5+} ratio and the specific surface area shows a stronger correlation with the rate of H_2 evolution (Figure S10b), giving a correlation coefficient of R^2 = 0.50. However, this value is much lower than that between the specific surface area and the H_2 evolution rate (R^2 = 0.83, see Figure 11). The R^2 values were analytically determined numbers of correlations between photocatalytic activity and certain parameters and had no further meaning. Nevertheless, the relative strength of the respective activity-parameter correlations can be compared. Anyway, the existence of the reduced Ta species appears to be a secondary factor that may affect the H_2 yield.

For layered mixed-anion compounds such as Sillén–Aurivillius oxyhalides, charge-carrier photoconductivity in the material bulk should play important roles in determining the photocatalytic activity.[59,60] Therefore, we evaluated the photogenerated charge carrier dynamics in $K_2LaTa_2O_6N$:*M* using TRMC measurements. Figure S11 shows the TRMC transient decay profiles for $K_2LaTa_2O_6N$:*M*. The signal intensity of $\varphi\Sigma\mu$ represents the photoconductivity of the $K_2LaTa_2O_6N$:*M*, and the decay reflects the lifetime of charge carriers. Undoped $K_2LaTa_2O_6N$ exhibited a $\varphi\Sigma\mu_{max}$ value of 3.0×10^{-7} m^2 V^{-1} s^{-1} and a half-lifetime ($\tau_{1/2}$) of 0.68 μs.

Table 3. Specific Surface Areas, $\varphi\Sigma\mu_{max}$, $\tau_{1/2}$, and Initial H_2 Evolution Rates for $K_2LaTa_2O_6N$:*M*

Sample	Specific surface area/m^2 g^{-1}	$\varphi\Sigma\mu_{max}$[a]/m^2 V^{-1} s^{-1} × 10^{-7}	$\tau_{1/2}$[a]/μs	Ta^{4+}/Ta^{5+}[b]	H_2 evolution rate[c]/μmol h^{-1}
$K_2LaTa_2O_6N$	2.4	3.0	0.68	2.0	4.0 ± 0.7
$K_2LaTa_2O_6N$:Mg (1 mol %)	4.1	2.0	0.56	3.4	5.2
$K_2LaTa_2O_6N$:Al (1 mol %)	3.5	3.2	0.33	0.5	5.0
$K_2LaTa_2O_6N$:Ga (1 mol %)	5.4	2.6	0.37	1.7	6.6 ± 0.9
$K_2LaTa_2O_6N$:Zr (1 mol %)	2.7	2.7	0.42	0.9	4.4
$K_2LaTa_2O_6N$:Mo (1 mol %)	2.1	1.7	0.62	3.0	3.1
$K_2LaTa_2O_6N$:W (1 mol %)	2.5	0.8	0.28	1.9	2.6
$K_2LaTa_2O_6N$:Ga (5 mol %)	6.1	1.2	0.61	0.6	9.0 ± 0.1
$K_2LaTa_2O_6N$:Ga (10 mol %)	6.6	1.6	0.35	0.8	15.1 ± 3.4
$K_2LaTa_2O_6N$:Ga (20 mol %)	6.7	1.1	0.24	0.4	11.3 ± 0.3

[a]From TRMC measurements. [b]Estimated by XPS (Figures S2 and S8). [c]The reaction conditions were the same as that in Figures 5 and 10.

https://doi.org/10.1021/acsaem.4c03131
ACS Appl. Energy Mater. 2025, 8, 3541−3552

Compared with the $\varphi\Sigma\mu_{max}$ value for the undoped material, that for $K_2LaTa_2O_6N$:Al was slightly higher; by contrast, those for the other doped samples were lower. In particular, $K_2LaTa_2O_6N$:W exhibited the lowest $\varphi\Sigma\mu_{max}$ value among the tested samples. The $\varphi\Sigma\mu_{max}$ and $\tau_{1/2}$ values are summarized in Table 3. We found that cation doping tended to negatively affect the photoconductivity and that the magnitude of the effect was greater for higher-valence cations (e.g., W). Similarly, $K_2LaTa_2O_6N$:Ga (1, 5, 10, 20 mol %) samples were measured (Figure S11b). As a general trend, the $\varphi\Sigma\mu_{max}$ value decreased with increasing Ga concentration, indicating that doping $K_2LaTa_2O_6N$ with Ga lowered the photoconductivity. More importantly, no strong correlation was found between the $\varphi\Sigma\mu_{max} \times \tau_{1/2}$ value and the H_2 evolution rate for $K_2LaTa_2O_6N$:*M* (Figure S12).

It is known that the particle size of cocatalyst has an impact on photocatalytic H_2 evolution activity.[7,27] As shown in Figure S13, the deposition of Pt on the $K_2LaTa_2O_6N$:M occurred in the form of ∼5 nm nanoparticles with some aggregations that formed larger secondary particles. Compared to Ga- and Mo-doped specimens that showed higher and lower photocatalytic activity, the average particle size of Pt in the former was 5.3 nm, which was larger than that in the latter (4.3 nm), as shown in Figure S14. In general, smaller Pt particle performs better as a H_2 evolution cocatalyst, compared to larger ones.[61] However, this was not the case in the doped $K_2LaTa_2O_6N$.

Thus, we concluded that the enlarged specific surface area is the primary contributor to the improved photocatalytic activity of $K_2LaTa_2O_6N$:*M* for visible-light H_2 evolution. However, we note that, despite a similar specific surface area, the $K_2LaTa_2O_6N$:Ga (20 mol %) sample showed lower activity than the 10 mol % sample (Table 3). This negative effect of the excess Ga dopant could be explained in terms of the absorption edge; as shown in Figure 9, increasing the Ga concentration from 10 to 20 mol % resulted in a substantial blueshift of the absorption edge, which is unfavorable for visible-light absorption. Nevertheless, transient absorption spectroscopy indicated that increasing the Ga concentration prolonged the lifetime of trapped charge carriers; that is, charge separation could be realized upon Ga doping (Figure S15).

In the bulk-type oxynitride photocatalysts, high surface area hardly contributes to high activity for H_2 evolution, because other factors govern the activity (in most cases, formation of reduced metal species and the concomitant generation of anionic defects).[4,22,27,40,41,58] In this respect, the present result showing a positive correlation between specific surface area and H_2 evolution activity of 2D $K_2LaTa_2O_6N$:*M* is peculiar. A characteristic feature of $K_2LaTa_2O_6N$ is the low nitrogen concentration in their chemical composition (i.e., only one nitrogen in the total of seven anions). On the other hand, the nitrogen concentration in the bulk-type perovskite oxynitrides (e.g., $BaTaO_2N$ and $LaTaON_2$) is relatively high. In other words, the Ta atoms in the perovskite block layer of $K_2LaTa_2O_6N$ interact more with oxygen rather than with nitrogen. This situation may suppress an excess reduction of Ta in $K_2LaTa_2O_6N$ during the topochemical nitridation synthesis, similar to ZrO_2-modified TaON,[4,27] although the absolute concentration of the reduced Ta species in the whole material could not be quantified due to the lack of a suitable technique. The fact that there is no correlation between the concentration of reduced Ta species estimated from XPS and photocatalytic activity of $K_2LaTa_2O_6N$:*M* strongly suggests that the concentration of reduced Ta species in the material is low enough not to affect the activity.

CONCLUSIONS

The effects of metal cations doping into a Ruddlesden–Popper-type layered oxynitride $K_2LaTa_2O_6N$ were examined as a potential method for improving its photocatalytic activity toward visible-light H_2 evolution. Doping with low-valence metal cations (e.g., Mg^{2+}, Al^{3+}, and Ga^{3+}) enhanced the photocatalytic activity of $K_2LaTa_2O_6N$. In the case of Ga doping, increasing the amount of dopant reduced the particle size of $K_2LaTa_2O_6N$ and improved charge separation. However, excessive doping adversely affected the photocatalytic activity by increasing the bandgap, which is disadvantageous in terms of visible-light absorption. The H_2 evolution AQY achieved with the optimized $K_2LaTa_2O_6N$:Ga (10 mol %) photocatalyst was 2.7 ± 0.4% at 420 nm, which is the highest AQY reported to date for a layered oxynitride photocatalyst.

For the Ta-based oxynitride photocatalysts reported thus far, suppressing the generation of reduced Ta species (e.g., Ta^{4+} and Ta^{3+}) produced during the synthesis has been considered critical for achieving high photocatalytic activity for H_2 evolution.[4,19,22,27,58] Although reduced Ta species have also been noted as a factor that adversely affects the H_2 evolution photocatalytic activity of undoped $K_2LaTa_2O_6N$,[28] the negative effect of reduced Ta species on the activity was much smaller in the cation-doped $K_2LaTa_2O_6N$. This finding provides a useful guide for the further development of not only Ta-based layered oxynitrides but also Nb-based ones as photocatalysts for visible-light H_2 evolution.

ASSOCIATED CONTENT

Supporting Information

The Supporting Information is available free of charge at https://pubs.acs.org/doi/10.1021/acsaem.4c03131.

Data for ionic radii of some metal cations (Table S1), XRF (Table S2, Figures S3 and S4), XANES (Figures S1 and S5), XPS (Figures S2, S6, S7 and S8), photocatalytic reaction and its correlation with physicochemical parameters (Figures S9, S10, and S12), TRMC (Figure S11), SEM (Figure S13), Pt size distribution curves (Figure S14), and transient absorption decay curves (Figure S15) (PDF)

AUTHOR INFORMATION

Corresponding Author

Kazuhiko Maeda − *Department of Chemistry, School of Science, Institute of Science Tokyo, Tokyo 152-8550, Japan; Research Center for Autonomous Systems Materialogy (ASMat), Institute of Science Tokyo, Yokohama, Kanagawa 226-8501, Japan;* orcid.org/0000-0001-7245-8318; Email: maeda@chem.sci.isct.ac.jp

Authors

Hideya Tsuchikado − *Department of Chemistry, School of Science, Institute of Science Tokyo, Tokyo 152-8550, Japan*

Shuji Anabuki − *Graduate School of Natural Science and Technology, Okayama University, Okayama 700-8530, Japan*

https://doi.org/10.1021/acsaem.4c03131
ACS Appl. Energy Mater. 2025, 8, 3541−3552

Ovidiu Cretu − *Electron Microscopy Group, National Institute for Materials Science (NIMS), Tsukuba, Ibaraki 305-0044, Japan;* orcid.org/0000-0002-1822-8172
Yuki Kinoshita − *Department of Chemical Science and Engineering, School of Materials and Chemical Technology, Institute of Science Tokyo, Tokyo 152-8550, Japan;* orcid.org/0009-0002-5190-7238
Masashi Hattori − *Institute of Integrated Research, Institute of Science Tokyo, Yokohama, Kanagawa 226-8503, Japan;* orcid.org/0000-0002-0644-5137
Yuta Shiroma − *Department of Chemistry, School of Science, Institute of Science Tokyo, Tokyo 152-8550, Japan*
Dongxiao Fan − *Institute of Materials Structure Science High Energy Accelerator Research Organization, Tsukuba, Ibaraki 305-0801, Japan;* Present Address: Japan Synchrotron Radiation Research Institute (JASRI), Kouto 1-1-1, Sayo-cho, Sayo-gun, Hyogo 679-5198, Japan
Megumi Okazaki − *Department of Chemistry, School of Science, Institute of Science Tokyo, Tokyo 152-8550, Japan;* orcid.org/0000-0003-1167-9453
Takuto Soma − *Department of Chemical Science and Engineering, School of Materials and Chemical Technology, Institute of Science Tokyo, Tokyo 152-8550, Japan;* orcid.org/0000-0001-8685-9606
Fumitaka Ishiwari − *Department of Applied Chemistry, Graduate School of Engineering, Osaka University, Suita, Osaka 565- 0871, Japan; Innovative Catalysis Science Division, Institute for Open and Transdisciplinary Research Initiatives (ICS-OTRI), Osaka University, Suita, Osaka 565-0871, Japan; Japan Science and Technology Agency (JST), PRESTO, Kawaguchi, Saitama 332-0012, Japan;* orcid.org/0000-0002-0200-4510
Shunsuke Nozawa − *Institute of Materials Structure Science High Energy Accelerator Research Organization, Tsukuba, Ibaraki 305-0801, Japan;* orcid.org/0000-0003-4977-6849
Toshiyuki Yokoi − *Institute of Integrated Research, Institute of Science Tokyo, Yokohama, Kanagawa 226-8503, Japan;* orcid.org/0000-0002-3315-3172
Michikazu Hara − *Institute of Integrated Research, Institute of Science Tokyo, Yokohama, Kanagawa 226-8503, Japan;* orcid.org/0000-0003-3450-5704
Koji Kimoto − *Electron Microscopy Group, National Institute for Materials Science (NIMS), Tsukuba, Ibaraki 305-0044, Japan;* orcid.org/0000-0002-3927-0492
Akira Yamakata − *Graduate School of Natural Science and Technology, Okayama University, Okayama 700-8530, Japan;* orcid.org/0000-0003-3179-7588
Akinori Saeki − *Department of Applied Chemistry, Graduate School of Engineering, Osaka University, Suita, Osaka 565-0871, Japan; Innovative Catalysis Science Division, Institute for Open and Transdisciplinary Research Initiatives (ICS-OTRI), Osaka University, Suita, Osaka 565-0871, Japan;* orcid.org/0000-0001-7429-2200

Complete contact information is available at: https://pubs.acs.org/10.1021/acsaem.4c03131

Author Contributions

H.T. performed the majority of the experiments with Y.S. and M.O. and wrote the manuscript with K.M.; S.A. and A.Y. conducted TAS measurements and analyzed the results; O.C. and K.K. conducted STEM observations and analyzed the results; Y.K. and T.S. conducted XRF measurements with H.T.; D.F. and S.N. conducted XAFS measurements with H.T.; M. Hattori and M. Hara conducted XPS measurements with H.T.; F.I. and A.S. conducted TRMC measurements with H.T.; T.Y. performed SEM observations. K.M. supervised the project. All authors contributed to the final version of the manuscript.

Notes

The authors declare no competing financial interest.

■ ACKNOWLEDGMENTS

This work was supported by Grants-in-Aid for Scientific Research on the Transformative Research Area (A) "Supra-ceramics" (JP22H05142, JP22H05148, and JP23H04626) and "Dynamic Exciton" (JP20H05836 and JP20H05838) from the Japan Society for the Promotion of Science (JSPS). Part of the research highlighted in this paper was supported by a JSPS Core-to-Core Program (JPJSCCA20200004), a JST-CREST program (JPMJCR20R2), and JST SPRING (JPMJSP2106). The authors thank Ms. Yuka Akimoto (Core Facility Center, Institute of Science Tokyo) for assistance in SEM observations.

■ REFERENCES

(1) Nishioka, S.; Osterloh, F. E.; Wang, X.; Mallouk, T. E.; Maeda, K. Photocatalytic water splitting. *Nat. Rev. Methods Primers* **2023**, *3* (1), 42.
(2) Takata, T.; Jiang, J.; Sakata, Y.; Nakabayashi, M.; Shibata, N.; Nandal, V.; Seki, K.; Hisatomi, T.; Domen, K. Photocatalytic water splitting with a quantum efficiency of almost unity. *Nature* **2020**, *581* (7809), 411−414.
(3) Scaife, D. E. Oxide semiconductors in photoelectrochemical conversion of solar energy. *Sol. Energy* **1980**, *25* (1), 41−54.
(4) Maeda, K.; Terashima, H.; Kase, K.; Higashi, M.; Tabata, M.; Domen, K. Surface Modification of TaON with Monoclinic ZrO_2 to Produce a Composite Photocatalyst with Enhanced Hydrogen Evolution Activity under Visible Light. *Bull. Chem. Soc. Jpn.* **2008**, *81* (8), 927−937.
(5) Maeda, K.; Lu, D.; Domen, K. Direct Water Splitting into Hydrogen and Oxygen under Visible Light by using Modified TaON Photocatalysts with d^0 Electronic Configuration. *Chem. -Eur. J.* **2013**, *19* (16), 4986−4991.
(6) Chen, K.; Xiao, J.; Vequizo, J. J. M.; Hisatomi, T.; Ma, Y.; Nakabayashi, M.; Takata, T.; Yamakata, A.; Shibata, N.; Domen, K. Overall Water Splitting by a $SrTaO_2N$-Based Photocatalyst Decorated with an Ir-Promoted Ru-Based Cocatalyst. *J. Am. Chem. Soc.* **2023**, *145* (7), 3839−3843.
(7) Wang, Z.; Luo, Y.; Hisatomi, T.; Vequizo, J. J. M.; Suzuki, S.; Chen, S.; Nakabayashi, M.; Lin, L.; Pan, Z.; Kariya, N.; Yamakata, A.; Shibata, N.; Takata, T.; Teshima, K.; Domen, K. Sequential cocatalyst decoration on $BaTaO_2N$ towards highly-active Z-scheme water splitting. *Nat. Commun.* **2021**, *12* (1), 1005.
(8) Liu, M.; You, W.; Lei, Z.; Takata, T.; Domen, K.; Li, C. Photocatalytic Water Splitting to Hydrogen over a Visible Light-Driven $LaTaON_2$ Catalyst. *Chin. J. Catal.* **2006**, *27* (7), 556−558.
(9) Hashiguchi, H.; Maeda, K.; Abe, R.; Ishikawa, A.; Kubota, J.; Domen, K. Photoresponse of GaN:ZnO Electrode on FTO under Visible Light Irradiation. *Bull. Chem. Soc. Jpn.* **2009**, *82* (3), 401−407.
(10) Lee, Y.; Terashima, H.; Shimodaira, Y.; Teramura, K.; Hara, M.; Kobayashi, H.; Domen, K.; Yashima, M. Zinc Germanium Oxynitride as a Photocatalyst for Overall Water Splitting under Visible Light. *J. Phys. Chem. C* **2007**, *111* (2), 1042−1048.
(11) Domen, K.; Kudo, A.; Tanaka, A.; Onishi, T. Overall photodecomposition of water on a layered niobiate catalyst. *Catal. Today* **1990**, *8* (1), 77−84.
(12) Domen, K.; Kudo, A.; Shinozaki, A.; Tanaka, A.; Maruya, K.; Onishi, T. Photodecomposition of water and hydrogen evolution

from aqueous methanol solution over novel niobate photocatalysts. *J. Chem. Soc., Chem. Commun.* **1986**, No. 4, 356.
(13) Takata, T.; Shinohara, K.; Tanaka, A.; Hara, M.; Kondo, J. N.; Domen, K. A highly active photocatalyst for overall water splitting with a hydrated layered perovskite structure. *J. Photochem. Photobiol. A Chem.* **1997**, *106* (1−3), 45−49.
(14) Ikeda, S.; Hara, M.; Kondo, J. N.; Domen, K.; Takahashi, H.; Okubo, T.; Kakihana, M. Preparation of $K_2La_2Ti_3O_{10}$ by Polymerized Complex Method and Photocatalytic Decomposition of Water. *Chem. Mater.* **1998**, *10* (1), 72−77.
(15) Machida, M.; Yabunaka, J.; Kijima, T. Synthesis and Photocatalytic Property of Layered Perovskite Tantalates, $RbLnTa_2O_7$ (Ln = La, Pr, Nd, and Sm). *Chem. Mater.* **2000**, *12* (3), 812−817.
(16) Schottenfeld, J. A.; Benesi, A. J.; Stephens, P. W.; Chen, G.; Eklund, P. C.; Mallouk, T. E. Structural analysis and characterization of layer perovskite oxynitrides made from Dion−Jacobson oxide precursors. *J. Solid State Chem.* **2005**, *178* (7), 2313−2321.
(17) Oshima, T.; Ichibha, T.; Qin, K. S.; Muraoka, K.; Vequizo, J. J. M.; Hibino, K.; Kuriki, R.; Yamashita, S.; Hongo, K.; Uchiyama, T.; Fujii, K.; Lu, D.; Maezono, R.; Yamakata, A.; Kato, H.; Kimoto, K.; Yashima, M.; Uchimoto, Y.; Kakihana, M.; Ishitani, O.; Kageyama, H.; Maeda, K. Undoped Layered Perovskite Oxynitride $Li_2LaTa_2O_6N$ for Photocatalytic CO_2 Reduction with Visible Light. *Angew. Chem., Int. Ed.* **2018**, *57* (27), 8154−8158.
(18) Oshima, T.; Ichibha, T.; Oqmhula, K.; Hibino, K.; Mogi, H.; Yamashita, S.; Fujii, K.; Miseki, Y.; Hongo, K.; Lu, D.; Maezono, R.; Sayama, K.; Yashima, M.; Kimoto, K.; Kato, H.; Kakihana, M.; Kageyama, H.; Maeda, K. Two-Dimensional Perovskite Oxynitride $K_2LaTa_2O_6N$ with an H^+/K^+ Exchangeability in Aqueous Solution Forming a Stable Photocatalyst for Visible-Light H_2 Evolution. *Angew. Chem., Int. Ed.* **2020**, *59* (24), 9736−9743.
(19) Maeda, K.; Domen, K. Water Oxidation Using a Particulate $BaZrO_3$-$BaTaO_2N$ Solid-Solution Photocatalyst That Operates under a Wide Range of Visible Light. *Angew. Chem., Int. Ed.* **2012**, *51* (39), 9865−9869.
(20) Sun, X.; Liu, G.; Xu, X. Defect management and efficient photocatalytic water oxidation reaction over Mg modified $SrNbO_2N$. *J. Mater. Chem.* **2018**, *6* (23), 10947−10957.
(21) Wu, F.; Sun, X.; Liu, G.; Xu, X. Actualizing efficient photocatalytic water oxidation over $SrTaO_2N$ by Na modification. *Catal. Sci. Technol.* **2017**, *7* (20), 4640−4647.
(22) Obata, K.; Higashi, T.; Ye, F.; Katayama, M.; Takanabe, K. Cation-Doped $SrTaO_2N$ Prepared through a Flux Method for Visible-Light-Driven Water Splitting. *ChemPhotoChem* **2023**, *7* (4), No. e202200293.
(23) Wang, Y.; Jin, S.; Pan, G.; Li, Z.; Chen, L.; Liu, G.; Xu, X. Zr doped mesoporous $LaTaON_2$ for efficient photocatalytic water splitting. *J. Mater. Chem.* **2019**, *7* (10), 5702−5711.
(24) Zhang, H.; Wei, S.; Xu, X. Mg modified $BaTaO_2N$ as an efficient visible-light-active photocatalyst for water oxidation. *J. Catal.* **2020**, *383*, 135−143.
(25) Hojamberdiev, M.; Vargas, R.; Kadirova, Z. C.; Kato, K.; Sena, H.; Krasnov, A. G.; Yamakata, A.; Teshima, K.; Lerch, M. Unfolding the Role of B Site-Selective Doping of Aliovalent Cations on Enhancing Sacrificial Visible Light-Induced Photocatalytic H_2 and O_2 Evolution over $BaTaO_2N$. *ACS Catal.* **2022**, *12* (2), 1403−1414.
(26) Maeda, K.; Lu, D.; Domen, K. Oxidation of Water under Visible-Light Irradiation over Modified $BaTaO_2N$ Photocatalysts Promoted by Tungsten Species. *Angew. Chem., Int. Ed.* **2013**, *52* (25), 6488−6491.
(27) Maeda, K.; Higashi, M.; Lu, D.; Abe, R.; Domen, K. Efficient Nonsacrificial Water Splitting through Two-Step Photoexcitation by Visible Light using a Modified Oxynitride as a Hydrogen Evolution Photocatalyst. *J. Am. Chem. Soc.* **2010**, *132* (16), 5858−5868.
(28) Mogi, H.; Kato, K.; Yasuda, S.; Kanazawa, T.; Miyoshi, A.; Nishioka, S.; Oshima, T.; Tang, Y.; Yokoi, T.; Nozawa, S.; Yamakata, A.; Maeda, K. Control of the Photocatalytic Activity of Metastable Layered Oxynitride $K_2LaTa_2O_6N$ through Topochemical Transformation of Tuned Oxide Precursors. *Chem. Mater.* **2021**, *33* (16), 6443−6452.
(29) Yoshida, H.; Pan, Z.; Shoji, R.; Nandal, V.; Matsuzaki, H.; Seki, K.; Hisatomi, T.; Domen, K. Heterogeneous doping of visible-light-responsive $Y_2Ti_2O_5S_2$ for enhanced hydrogen evolution. *J. Mater. Chem. A* **2022**, *10* (46), 24552−24560.
(30) Takata, T.; Domen, K. Defect Engineering of Photocatalysts by Doping of Aliovalent Metal Cations for Efficient Water Splitting. *J. Phys. Chem. C* **2009**, *113* (45), 19386−19388.
(31) Zhao, Z.; Goncalves, R. V.; Barman, S. K.; Willard, E. J.; Byle, E.; Perry, R.; Wu, Z.; Huda, M. N.; Moulé, A. J.; Osterloh, F. E. Electronic structure basis for enhanced overall water splitting photocatalysis with aluminum doped $SrTiO_3$ in natural sunlight. *Energy Environ. Sci.* **2019**, *12* (4), 1385−1395.
(32) Iwase, A.; Kato, H.; Kudo, A. The Effect of Alkaline Earth Metal Ion Dopants on Photocatalytic Water Splitting by $NaTaO_3$ Powder. *ChemSusChem* **2009**, *2* (9), 873−877.
(33) Kudo, A.; Kato, H. Effect of lanthanide-doping into $NaTaO_3$ photocatalysts for efficient water splitting. *Chem. Phys. Lett.* **2000**, *331* (5−6), 373−377.
(34) Alves, G. A. S.; Centurion, H. A.; Sambrano, J. R.; Ferrer, M. M.; Gonçalves, R. V. Band Gap Narrowing of Bi-Doped $NaTaO_3$ for Photocatalytic Hydrogen Evolution under Simulated Sunlight: A Pseudocubic Phase Induced by Doping. *ACS Appl. Energy Mater.* **2021**, *4* (1), 671−679.
(35) Shiroma, Y.; Mogi, H.; Mashiko, T.; Yasuda, S.; Nishioka, S.; Yokoi, T.; Ida, S.; Kimoto, K.; Maeda, K. Interlayer modification and single-layer exfoliation of the Ruddlesden−Popper perovskite oxynitride $K_2LaTa_2O_6N$ to improve photocatalytic H_2 evolution activity. *J. Mater. Chem.* **2023**, *11* (17), 9485−9492.
(36) Ravel, B.; Newville, M. ATHENA, ARTEMIS, HEPHAESTUS: Data analysis for X-ray absorption spectroscopy using IFEFFIT. *J. Synchrotron Rad.* **2005**, *12* (4), 537−541.
(37) Aihara, K.; Mizuochi, R.; Okazaki, M.; Nishioka, S.; Yasuda, S.; Yokoi, T.; Ishiwari, F.; Saeki, A.; Inada, M.; Maeda, K. Low-Temperature Microwave-Assisted Hydrothermal Synthesis of $Pb_2Ti_2O_{5.4}F_{1.2}$ Photocatalyst for Improved H_2 Evolution under Visible Light. *ACS Mater. Lett.* **2023**, *5* (9), 2355−2360.
(38) Yamakata, A.; Ishibashi, T.; Onishi, H. Water- and Oxygen-Induced Decay Kinetics of Photogenerated Electrons in TiO_2 and Pt/TiO_2: A Time-Resolved Infrared Absorption Study. *J. Phys. Chem. B* **2001**, *105* (30), 7258−7262.
(39) Tang, Y.; Kato, K.; Oshima, T.; Mogi, H.; Miyoshi, A.; Fujii, K.; Yanagisawa, K.; Kimoto, K.; Yamakata, A.; Yashima, M.; Maeda, K. Synthesis of Three-Layer Perovskite Oxynitride $K_2Ca_2Ta_3O_9N{\cdot}2H_2O$ and Photocatalytic Activity for H_2 Evolution under Visible Light. *Inorg. Chem.* **2020**, *59* (15), 11122−11128.
(40) Maeda, K.; Terashima, H.; Kase, K.; Domen, K. Nanoparticulate precursor route to fine particles of TaON and ZrO_2−TaON solid solution and their photocatalytic activity for hydrogen evolution under visible light. *Appl. Catal., A* **2009**, *357* (2), 206−212.
(41) Maeda, K.; Domen, K. Preparation of $BaZrO_3$−$BaTaO_2N$ solid solutions and the photocatalytic activities for water reduction and oxidation under visible light. *J. Catal.* **2014**, *310*, 67−74.
(42) Anzai, A.; Fujiwara, K.; Yamamoto, A.; Yoshida, H. Platinum-loaded lanthanum-doped calcium titanate photocatalysts prepared by a flux method for photocatalytic steam reforming of methane. *Catal. Today* **2020**, *352*, 1−9.
(43) Burn, I.; Neirman, S. Dielectric properties of donor-doped polycrystalline $SrTiO_3$. *J. Mater. Sci.* **1982**, *17* (12), 3510−3524.
(44) Hui, S.; Petric, A. Evaluation of yttrium-doped $SrTiO_3$ as an anode for solid oxide fuel cells. *J. Eur. Ceram. Soc.* **2002**, *22* (9), 1673−1681.
(45) Peng, C. J.; Chiang, Y. M. Grain growth in donor-doped $SrTiO_3$. *J. Mater. Res.* **1990**, *5* (6), 1237−1245.
(46) Chun, W. J.; Ishikawa, A.; Fujisawa, H.; Takata, T.; Kondo, J. N.; Hara, M.; Kawai, M.; Matsumoto, Y.; Domen, K. Conduction and Valence Band Positions of Ta_2O_5, TaON, and Ta_3N_5 by UPS and

https://doi.org/10.1021/acsaem.4c03131
ACS Appl. Energy Mater. 2025, 8, 3541−3552

Electrochemical Methods. *J. Phys. Chem. B* **2003**, *107* (8), 1798−1803.
(47) Li, H.; Xiao, J.; Vequizo, J. J. M.; Hisatomi, T.; Nakabayashi, M.; Pan, Z.; Shibata, N.; Yamakata, A.; Takata, T.; Domen, K. One-Step Excitation Overall Water Splitting over a Modified Mg-Doped $BaTaO_2N$ Photocatalyst. *ACS Catal.* **2022**, *12* (16), 10179−10185.
(48) Pennycook, S. J.; Jesson, D. E. High-resolution Z-contrast imaging of crystals. *Ultramicroscopy* **1991**, *37* (1−4), 14−38.
(49) Nishi, K.; Shimizu, K.; Takamatsu, M.; Yoshida, H.; Satsuma, A.; Tanaka, T.; Yoshida, S.; Hattori, T. Deconvolution Analysis of Ga K-Edge XANES for Quantification of Gallium Coordinations in Oxide Environments. *J. Phys. Chem. B* **1998**, *102* (50), 10190−10195.
(50) Scharmann, F.; Cherkashinin, G.; Breternitz, V.; Knedlik, C.; Hartung, G.; Weber, T.; Schaefer, J. A. Viscosity effect on GaInSn studied by XPS. *Surf. Interface Anal.* **2004**, *36* (8), 981−985.
(51) Shrestha, N. K.; Bui, H. T.; Lee, T.; Noh, Y. Y. Interfacial Engineering of Nanoporous Architectures in Ga_2O_3 Film toward Self-Aligned Tubular Nanostructure with an Enhanced Photocatalytic Activity on Water Splitting. *Langmuir* **2018**, *34* (15), 4575−4583.
(52) Tran, N. H.; Holzschuh, W. J.; Lamb, R. N.; Lai, L. J.; Yang, Y. W. Structural Order in Oxygenated Gallium Nitride Films. *J. Phys. Chem. B* **2003**, *107* (35), 9256−9260.
(53) Grodzicki, M. Properties of Thin Film-Covered GaN(0001) Surfaces. *Mater. Proc.* **2020**, *2* (1), 30.
(54) Hara, S.; Yoshimizu, M.; Tanigawa, S.; Ni, L.; Ohtani, B.; Irie, H. Hydrogen and Oxygen Evolution Photocatalysts Synthesized from Strontium Titanate by Controlled Doping and Their Performance in Two-Step Overall Water Splitting under Visible Light. *J. Phys. Chem. C* **2012**, *116* (33), 17458−17463.
(55) Maeda, K.; Abe, R.; Domen, K. Role and Function of Ruthenium Species as Promoters with TaON-Based Photocatalysts for Oxygen Evolution in Two-Step Water Splitting under Visible Light. *J. Phys. Chem. C* **2011**, *115* (7), 3057−3064.
(56) Higashi, M.; Abe, R.; Takata, T.; Domen, K. Photocatalytic Overall Water Splitting under Visible Light Using $ATaO_2N$ (A = Ca, Sr, Ba) and WO_3 in a IO_3^-/I^- Shuttle Redox Mediated System. *Chem. Mater.* **2009**, *21* (8), 1543−1549.
(57) Nishioka, S.; Shibata, K.; Miseki, Y.; Sayama, K.; Maeda, K. Visible-light-driven nonsacrificial hydrogen evolution by modified carbon nitride photocatalysts. *Chin. J. Catal.* **2022**, *43* (9), 2316−2320.
(58) Sasaki, R.; Maeda, K.; Kako, Y.; Domen, K. Preparation of calcium tantalum oxynitride from layered oxide precursors to improve photocatalytic activity for hydrogen evolution under visible light. *Appl. Catal., B* **2012**, *128* (30), 72−76.
(59) Ogawa, K.; Suzuki, H.; Zhong, C.; Sakamoto, R.; Tomita, O.; Saeki, A.; Kageyama, H.; Abe, R. Layered Perovskite Oxyiodide with Narrow Band Gap and Long Lifetime Carriers for Water Splitting Photocatalysis. *J. Am. Chem. Soc.* **2021**, *143* (22), 8446−8453.
(60) Suzuki, H.; Higashi, M.; Kunioku, H.; Abe, R.; Saeki, A. Photoconductivity−Lifetime Product Correlates Well with the Photocatalytic Activity of Oxyhalides Bi_4TaO_8Cl and $PbBiO_2Cl$: An Approach to Boost Their O_2 Evolution Rates. *ACS Energy Lett.* **2019**, *4* (7), 1572−1578.
(61) Oshima, T.; Lu, D.; Ishitani, O.; Maeda, K. Intercalation of Highly Dispersed Metal Nanoclusters into a Layered Metal Oxide for Photocatalytic Overall Water Splitting. *Angew. Chem., Int. Ed.* **2015**, *127* (9), 2736−2740.

https://doi.org/10.1021/acsaem.4c03131
ACS Appl. Energy Mater. 2025, 8, 3541−3552